Progress in Additive Manufacturing
https://doi.org/10.1007/s40964-026-01938-8

RESEARCH

Spatter-based in situ monitoring of process variability in PBF-LB/M with application to NiTi shape memory alloy

Hang Zheng[1] · Marco Grasso[1] · Tiziana Biasutti[2] · Adelaide Nespoli[3] · Antonio Mattia Grande[2] · Paolo Bettini[2] · Giuseppe Sala[2] · Bianca Maria Colosimo[1]

Received: 30 April 2026 / Accepted: 19 August 2026
© The Author(s) 2026

Abstract
In situ monitoring in metal laser powder bed fusion (PBF-LB/M) is increasingly used not only for anomaly detection but also for material development and process optimization. Among available process signatures, spatter ejections have been widely studied, though mainly in relation to process parameters and energy density. This work investigates how spatter dynamics can capture additional and often overlooked sources of variability, including spatial variations within layers and geometry-induced changes across layers. Detecting such multi-scale variations is essential to ensure consistent part quality, particularly for materials with narrow process windows. The proposed approach is applied to the PBF-LB/M of NiTi, a crack-prone alloy with pseudo-elastic and shape memory properties and high sensitivity to process instabilities. A case study on structural NiTi dampers shows that spatter descriptors effectively capture process variations induced by powder spreading irregularities and evolving geometry along the build direction. The results highlight the potential of spatter-based monitoring to support the early identification of process deviations and defect-prone conditions in process-sensitive materials.

Keywords In situ monitoring · Spatters · Shape memory alloy · NiTi · Laser powder bed fusion · Additive manufacturing

✉ Marco Grasso
marcoluigi.grasso@polimi.it

Hang Zheng
hang.zheng789@gmail.com

Tiziana Biasutti
tiziana.biasutti@polimi.it

Adelaide Nespoli
adelaide.nespoli@cnr.it

Antonio Mattia Grande
antoniomattia.grande@polimi.it

Paolo Bettini
paolo.bettini@polimi.it

Giuseppe Sala
giuseppe.sala@polimi.it

Bianca Maria Colosimo
biancamaria.colosimo@polimi.it

[1] Department of Mechanical Engineering, Politecnico di Milano, Milan, Italy

[2] Department of Aerospace Science and Technology, Politecnico di Milano, Milan, Italy

[3] CNR-ICMATE, Institute of Condensed Matter Chemistry and Technologies for Energy, Lecco, Italy

1 Introduction

The metal laser powder bed fusion (PBF-LB/M) process, like other metal additive manufacturing (AM) technologies, is inherently affected by multiple sources of variability, leading to fluctuations within and across layers. These include non-uniform heat dissipation, instabilities in laser–material interaction, contamination, and powder spreading irregularities, which may arise even under nominally optimal conditions due to stochastic perturbations or evolving geometry.

In situ monitoring has therefore attracted increasing interest for anomaly detection, waste reduction, adaptive control, and process/material development [1–7]. Among available process signatures, material ejections, namely spatters and plume formations, have been extensively investigated as observable manifestations of melt pool dynamics [8–16]. Previous studies have mainly focused on their dependence on process parameters such as laser power, scan speed, and energy density, highlighting correlations with melt pool instability and defect formation [10–13]. Other works have

Published online: 08 September 2026

emphasized the role of process atmosphere, including gas flow and chamber pressure, in governing spatter transport and redeposition [14–16].

While these studies established the sensitivity of spatter signatures to nominal processing conditions, comparatively limited attention has been devoted to their capability to capture other relevant and often unavoidable sources of process variability arising during a build. These include location-dependent effects within the build plane, such as those associated with powder-spreading inhomogeneity and local recoating conditions, as well as geometry-dependent variations across layers associated with changes in exposed area and heat dissipation. The present study extends spatter-based monitoring to these sources of variability, rather than focusing exclusively on variations induced by nominal process parameters.

Moreover, most studies on spatter analysis and monitoring rely on simplified experimental configurations, such as single tracks or simple geometries, which are not representative of industrial builds involving multiple parts and evolving geometries. In realistic PBF-LB/M conditions, spatter analysis becomes particularly challenging. Multiple heat sources generate overlapping thermal emissions, while constrained viewing angles limit reliable detection and tracking. As a result, advanced spatter tracking approaches are often difficult to apply in industrial environments.

These limitations highlight the need for robust monitoring strategies capable of extracting meaningful process signatures under constrained acquisition conditions. Rather than relying on complete spatter trajectory reconstruction, the present study introduces a tracking-free monitoring strategy specifically designed for realistic multi-part build conditions. The approach restricts the analysis to ejecta detected within a defined neighborhood of the laser-heated zone, enabling near-origin spatter size, number, and ejection rate to be quantified as process signatures of both within-layer and across-layer variability. Focusing on near-origin spatters also reduces the influence of their subsequent transport by the macroscopic chamber cross-flow. Indeed, spatter trajectories are progressively affected by the shielding-gas flow as ejecta move away from their point of origin [17–19]. Characterizing ejecta close to the laser–material interaction zone is therefore expected to provide measurements that are less sensitive to downstream transport while retaining information on the local melt-pool, vapor-plume, and particle-entrainment dynamics responsible for their generation. In addition, the approach captures ejecta remaining in the vicinity of the processed region, which may locally redeposit and potentially affect part quality.

Capturing process variability both within and across layers is particularly critical for materials characterized by narrow processing windows. Shape memory alloys (SMAs) represent a prominent example. These advanced materials undergo reversible phase transformations that enable pseudo-elasticity and shape memory effects [20], making them attractive for applications ranging from space and aerospace to healthcare and automotive systems. Among SMAs, equiatomic Nitinol (NiTi) is particularly attractive because of its high specific actuation capability, biocompatibility, and resistance to thermal and mechanical cycling.

NiTi pseudo-elasticity enables the recovery of large deformations, up to 8%, through mechanical hysteresis associated with the transformation from austenite to stress-induced martensite during loading and the reverse transformation during unloading [21, 22]. This behavior makes NiTi particularly suitable for damping structures capable of absorbing dynamic loads without requiring complex and heavy kinematic solutions, an advantage of particular interest for space and aerospace applications [23, 24].

Despite these attractive functional properties, the PBF-LB/M processing of NiTi remains challenging because of its narrow processing window, high sensitivity to process variations, and susceptibility to crack formation [23–25]. This combination of functional relevance and process sensitivity makes NiTi a particularly suitable case study for assessing the capability of in situ monitoring strategies to capture subtle variations in process conditions. To the best of the authors' knowledge, spatter-related phenomena have not yet been systematically investigated in PBF-LB/M of NiTi.

The present study contributes to the literature in three main ways: (i) it provides the first investigation of spatter-based monitoring applied to NiTi; (ii) it highlights the role of location- and geometry-induced variability on spatter descriptors; and (iii) it proposes a methodology compatible with industrially representative conditions and transferable to other materials and systems.

2 Materials and methods

The experimental study involved the production of NiTi dampers whose nominal geometry is shown in Fig. 1. The damper has an overall height of 48.54 mm and consists of a modified octahedral cell designed to combine pseudo-elastic material behavior with enhanced damping capability [25]. The minimum cross-sectional area is approximately 7.04 mm^2.

The NiTi dampers were manufactured using a Renishaw AM400 equipped with a 400 W Ytterbium fibre laser with a spot diameter of approximately 70 μm at the focal point. Parts were built on a NiTi baseplate (78 × 78 mm), without preheating, using the reduced build volume (RBV) configuration. Powder spreading is performed by a metal recoater blade equipped with a silicone insert at the powder-contact

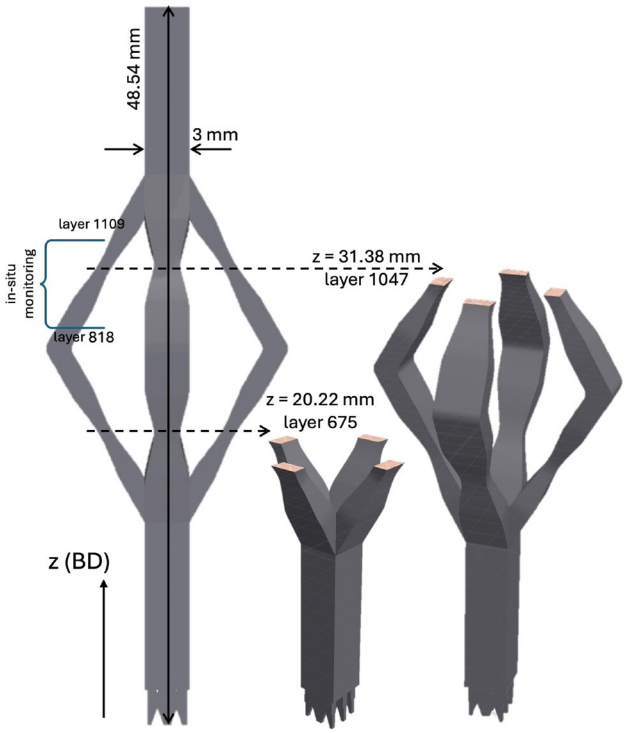

Fig. 1 NiTi damper geometry with modified octahedral cell used as reference geometry in this study; the in situ monitored region during the PBF-LB/M process spans from layer 818 to layer 1109 where major cross-section variation takes place

Table 1 Process parameters used in the PBF-LB/M experimentation (hatch distance and layer thickness were equal for all samples and set at H = 0.12 mm and z = 0.03 mm, respectively)

Part number (left-right)	Laser power (W)	Scan speed (mm/s)	Linear energy density (J/mm)
7 & 2	60	100	0.6
3 & 8	60	400	0.15
1 & 6	100	250	0.4
4 & 9	140	100	1.4
10 & 5	140	400	0.35

edge. The chamber was maintained under argon with oxygen content below 500 ppm. Gas-atomized NiTi powder supplied by Nanoval GmbH was used, with particle size ranging from 20 to 50 µm and reported d_{50} of 24.5 µm. The nominal composition of the powder was 50.8 at. % of Ni, balance Ti. The powder was not virgin, but scanning electron microscopy and differential scanning calorimetry performed before the build showed no major change with respect to the powder properties in its virgin state.

It should also be noted that powder characteristics, and particularly the powder size distribution (PSD), may influence particle entrainment and spatter ejection dynamics and, consequently, the spatter descriptors considered in this study. PSD was not investigated as an experimental factor here, as the same powder feedstock was used throughout the experimental campaign. The observed variations therefore refer to process variability occurring under nominally unchanged feedstock conditions.

Five different parameter sets were tested (Table 1), varying laser power and scan speed while keeping hatch distance and layer thickness fixed at H = 0.12 mm and z = 0.03 mm, respectively. A meander hatch pattern was applied, where adjacent scan tracks were processes in alternating directions. The hatch rotation angle was set to 67°. Two border scans were executed following an inside-out sequence, with a border offset of 0.1 mm. Two copies of the same geometry were manufactured for each parameter set. The production of specimens 4 and 9, corresponding to the highest energy density, was aborted at layer 725 due to severe overheating, whose effects on the solidified surface could interfere with powder spreading and propagate to other samples. The analysis was therefore limited to the remaining 8 samples.

The parameter selection was based on previous experiments with similar geometries and the same material, which showed that a linear energy density (LED) of 0.4 J/mm (P = 100 W, S = 250 mm/s) was suitable for achieving desirable pseudo-elastic properties. Both nominal and deliberately non-optimal conditions were therefore considered. The replication of identical geometries under the same parameters was designed to assess whether location-dependent effects within the build area could affect in situ process signatures and final part quality independently of the selected parameter set.

In the RBV configuration, the amount of powder delivered at each layer cannot be directly controlled. Instead, the pre-loaded and compacted powder feed volume is incrementally raised by one nominal layer thickness before each recoating step, and the resulting amount of powder is spread across the build area by the recoater. This configuration may result in spatially non-uniform powder deposition, as consistently observed in preliminary builds, where poorer powder coverage tended to occur on one side of the reduced build area. This known behavior of the RBV/recoating system was deliberately exploited in the present experiment to introduce a location-dependent perturbation in powder-bed coverage. Post-recoating images confirmed the expected asymmetry, as discussed in the following.

For each pair of samples manufactured with identical process parameters, one specimen was placed in the left-hand region and the other in the right-hand region of the build area. The allocation within each region was randomized to avoid systematic bias. The arrangement of the ten samples within the predefined grid is shown in Fig. 2.

Although not deterministically reproducible, non-uniform spreading conditions are representative of realistic PBF-LB/M process variability, where powder layer

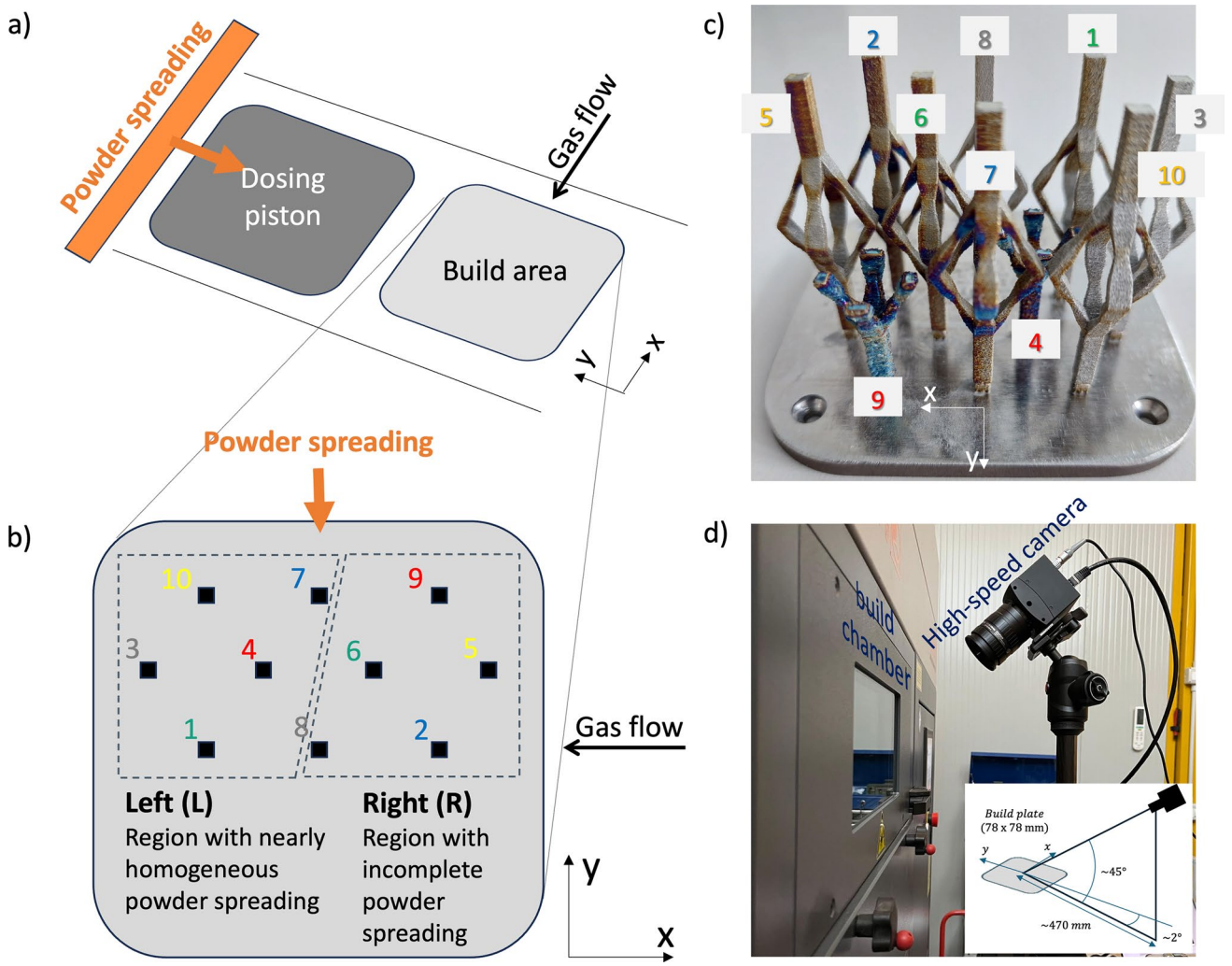

Fig. 2 **a** schematic view of the RBV system composed by a dosing piston and the reduced build area adopted in the study; **b** sample location within the build area with a schematic indication of regions characterized by a different quality of the powder spreading; **c** as-built samples before removal from the baseplate; **d** high-speed video imaging setup for in situ monitoring from the front viewport of the machine

inhomogeneities arise from multiple interacting factors and often affect localized build regions. The NiTi damper geometry introduced an additional source of variability through cross-section variation along the build direction, complementing process-parameter and location effects and enriching the analysis of spatter-related information.

In situ high-speed imaging was performed using an I-speed 220 camera placed outside the AM400 front door, as shown in Fig. 2d. Videos were acquired at 800 fps using a 50-mm macro lens, providing a spatial resolution of about 75.8 µm/pixel. A shutter time of 100 µs was used to minimize laser-motion blur, and no background illumination was applied. The camera was placed with a viewing angle of about 45° in elevation with respect to the baseplate, and about 2° in azimuth with respect to the reference system centred in the middle of the baseplate (as shown in the Fig. 2d).

The lateral extent of the monitored build area (78 mm) was relatively small compared with the camera-to-build distance (approximately 470 mm). As a result, the variation in viewing distance between the left- and right-hand portions of the monitored area was limited to less than 5 mm. Based on this, perspective- and distance-related optical effects were assumed to have only a minor influence on left-right differences of in situ measured quantities, although their contribution cannot be entirely excluded.

These settings enabled the complete laser scanning process of each recorded layer to be captured. A total of 18 layers, from layer 818 to layer 1109, were acquired during fabrication of the modified octahedral geometry. Precisely, monitored layers consisted of layers 818, 840, 850, 860, 870, 890, 905, 920, 937, 952, 964, 1036, 1047, 1053, 1065, 1077, 1087, and 1109. The non-continuous acquisition of consecutive layers resulted from the time required to save

each high-speed video before a new acquisition could be initiated. Consequently, intermediate layers were processed while the previously acquired video was being transferred and stored. Within the monitored portion of the build, the cross-section shrank to its minimum area, representing a critical condition for process stability because shorter inter-layer cooling times increase the risk of heat accumulation. This may promote overheating, swelling, and volumetric or microstructural variations detrimental to final part quality and functionality. The monitored layer range was therefore specifically selected to capture this progressive change in cross-sectional area and assess whether the resulting geometry-induced variation could be detected through the investigated in situ process signatures.

After fabrication, the as-built parts were inspected via X-ray CT using a Phoenix v|tomex|x m 300 kV system with a resolution of 0.02 mm. Volumetric defects such as micro-cracks, keyhole porosity, and lack-of-fusion porosity are known to degrade or even prevent pseudo-elastic behavior [26, 27], motivating the use of this non-destructive inspection method.

The scope of this work is to investigate the link between process variability and in situ spatter-based process signatures. Volumetric defects were therefore used to verify whether the observed process variations affected final part quality and integrity. The analysis does not include local compositional deviations, such as Ni evaporation, microstructural heterogeneities or precipitate formation, which may also influence NiTi functional response. A comprehensive assessment of functional performance is beyond the scope of this study and will be addressed in future work through compositional, microstructural, and functional characterization.

2.1 Video image processing and analysis

The proposed image processing workflow is summarized in Fig. 3. Let N be the number of parts exposed within a layer, with N = 8 in this study. Foreground regions in each video frame may include:

- The laser heated zone (LHZ) of the i-th part, namely a region that includes the melt pool and its hot surroundings whose emission in the visible range of radiation wavelengths is captured by the camera;
- The vapor plume emitted from the melt pool of the i-th part (i=1,..., N);
- One or more spatters ejected while the laser was scanning the i-th part;
- One or more spatters ejected while the laser was scanning the j-th part, with $i \neq j$;
- Other hot areas of the build, either belonging to the currently scanned i-th part or other parts previously scanned by the laser.

Each frame consists of a dark background and multiple bright foreground regions. Raw images (Fig. 3a) were converted to grayscale (Fig. 3b) and binarized using Otsu's algorithm to isolate connected components (Fig. 3c). The LHZ was automatically identified using two criteria. First, the largest component had to exceed an area threshold of 5 pixels, selected by visual inspection of trial calibration layers, to confirm that the laser was on. Second, the largest component had to contain at least one pixel above 95% of the saturation intensity, since the LHZ is directly heated by the laser and is expected to exhibit the highest brightness. Only when both criteria were satisfied, the largest

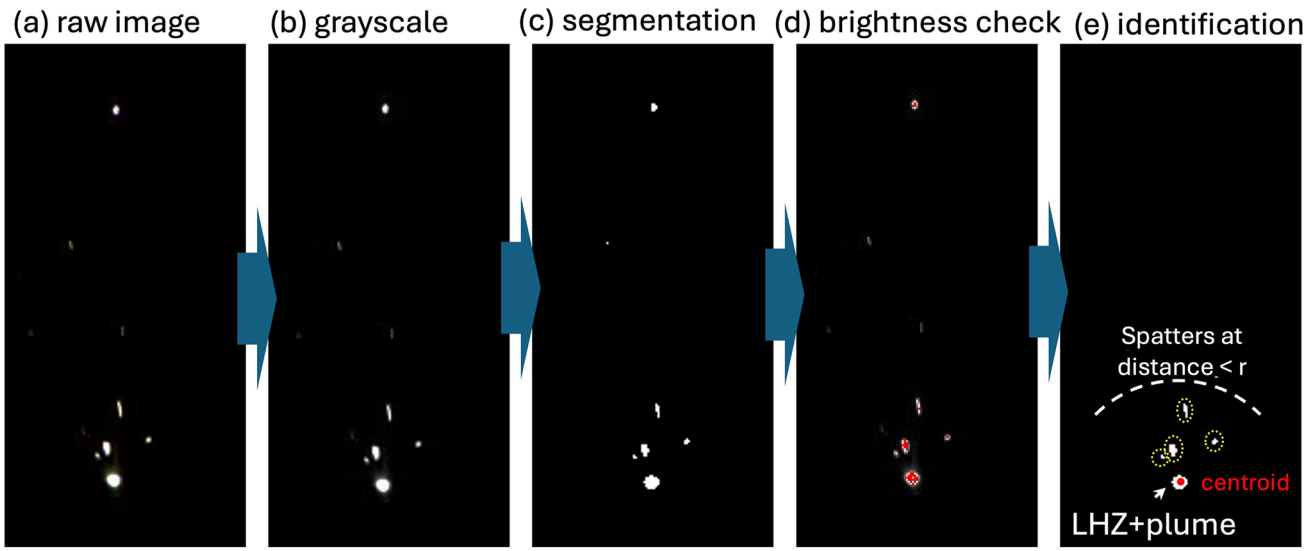

Fig. 3 Schematic view of the sequential steps for video image processing and estimation of near-origin spatter descriptors in addition to the area of the laser heated zone (possibly comprising also the plume in the visible range)

component was labeled as LHZ; otherwise, the frame was discarded as laser-off. If the LHZ was detected, all other components in the frame were labeled as spatters. Because the vapor plume, when visible, partially overlaps with the LHZ and cannot be reliably separated, their union is hereafter referred to as "LHZ+plume".

The separation between LHZ+plume and spatters follows the approach of Repossini et al. [10] and subsequent studies, where the largest region whose centroid lies within the exposed area is labeled as LHZ+plume. However, in complex builds, it is also necessary to limit spatter misclassification, mislabeling among different parts, and repeated counting of spatters visible over multiple consecutive frames.

Spatter tracking has been proposed to address these issues [8, 11–13], but it typically requires high frame rates, simplified builds with limited overlapping emissions, and favorable viewing angles. These conditions are rarely satisfied in industrial setups. In this study, the acquisition configuration was intentionally representative of a constrained industrial scenario with multiple parts and evolving geometries. Moreover, due to the viewing angle of the camera, spatters moving far from the exposure region rapidly went out of focus, limiting conventional tracking.

An alternative strategy was therefore adopted by identifying only spatters within a radius r from the LHZ centroid, hereafter referred to as *near-origin spatters*. This class includes both low-kinetic-energy spatters remaining close to the origin and faster spatters captured shortly after ejection. Restricting the analysis to near-origin spatters reduces mislabeling, repeated counting, and the inclusion of unrelated hot spots, while focusing on ejecta more likely to redeposit and affect local process conditions and part quality. In this study, $r = 30$ pixels was selected based on part spacing and camera spatial resolution.

Once regions of interest (ROIs) were isolated and labeled frame by frame, the following quantities were computed:

- LHZ+plume area, centroid and brightness (average pixel intensity)
- Area of near-origin spatters
- Number of near-origin spatters
- Near-origin spatter rate

The near-origin spatter rate was computed as the ratio between the number of frames containing at least one detected near-origin spatter and the total number of frames acquired during exposure of the region of interest. It represents a proxy for spatter ejection frequency and accounts for variations in the exposed area across layers by normalizing the number of ejected spatters by the corresponding exposure duration.

To quantify spatial inhomogeneities in powder recoating and verify differences between the left- and right-hand sides of the build area, powder bed images were acquired before and after laser exposure at selected layers using the same camera. ROIs corresponding to the solidified layers were identified in each image pair. Post-recoating images were then segmented to isolate connected components associated with super-elevated edges and locally uncovered surfaces. For each ROI of nominal area A_i, and denoting by A_i^* the corresponding uncoated area, the percentage of effective surface recoating was computed as $100 * (A_i - A_i^*)/A_i$.

Segmentation of post-recoating images was performed using a two-sided Otsu thresholding approach to capture regions either brighter or darker than the surrounding powder bed. The resulting regions were merged within each ROI to provide a unified representation of recoating irregularities.

3 Results

3.1 In situ characterization

An example of post-recoating images in ROIs centred on each specimen is shown in Fig. 4. Figure 4 refers to layer 850, within the portion of the build with constant cross-section area. Areas with pixel intensities brighter and darker than the loose powder background indicate super-elevated regions of the previously solidified layer. The extension of these regions is more evident for the samples manufactured on the right-hand side of the build area, with the only exception of samples 2 and 7, where super-elevated areas are of comparable extension in this specific layer.

Figure 5a reports bar plots with $\pm 3\,\sigma$ intervals of the mean percentage of surface recoating for samples manufactured on the left- and right-hand side of the build area. The top panel refers to layers 818–964, where the sample cross-section was nearly constant, whereas the bottom panel refers to layers 1036–1109, where the cross-section approached its minimum. Table 2 shows the results of pairwise statistical comparisons for mean percentages of surface recoating. Two-sample Student's t-tests with pooled variance were performed with familywise significance level of $\alpha = 0.05$ and Bonferroni's correction. The results of the test confirm a significant location effect in the first layer range, with more homogeneous recoating on the left-hand side. When the cross-section decreased, recoating worsened on both sides and no statistically significant left–right difference was observed apart for the pair of samples 3 and 4. This was likely caused by a general worsening of the superelevation of solidified surfaces when scan tracks became shorter, hindering proper layer deposition. Thus, Fig. 5a highlights both

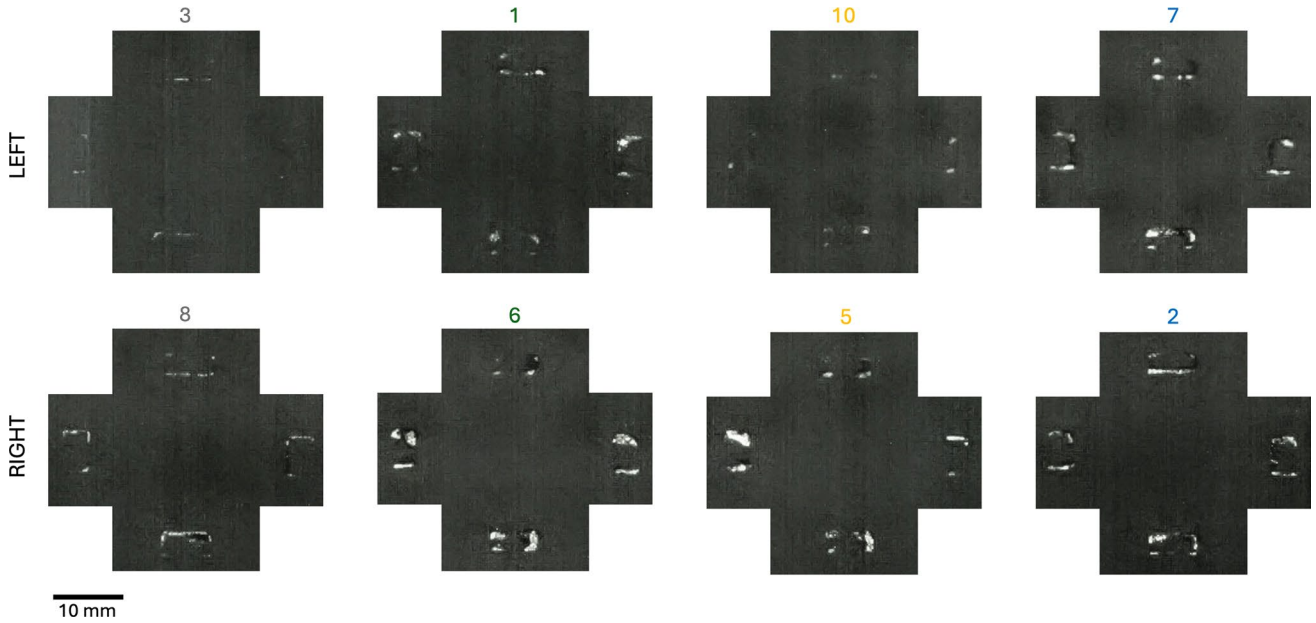

Fig. 4 Example of post-recoating images in layer 850 in ROIs corresponding to individual samples placed in the left-hand side (top) and right-hand side (bottom) of the build area. The sample index is indicated above each panel

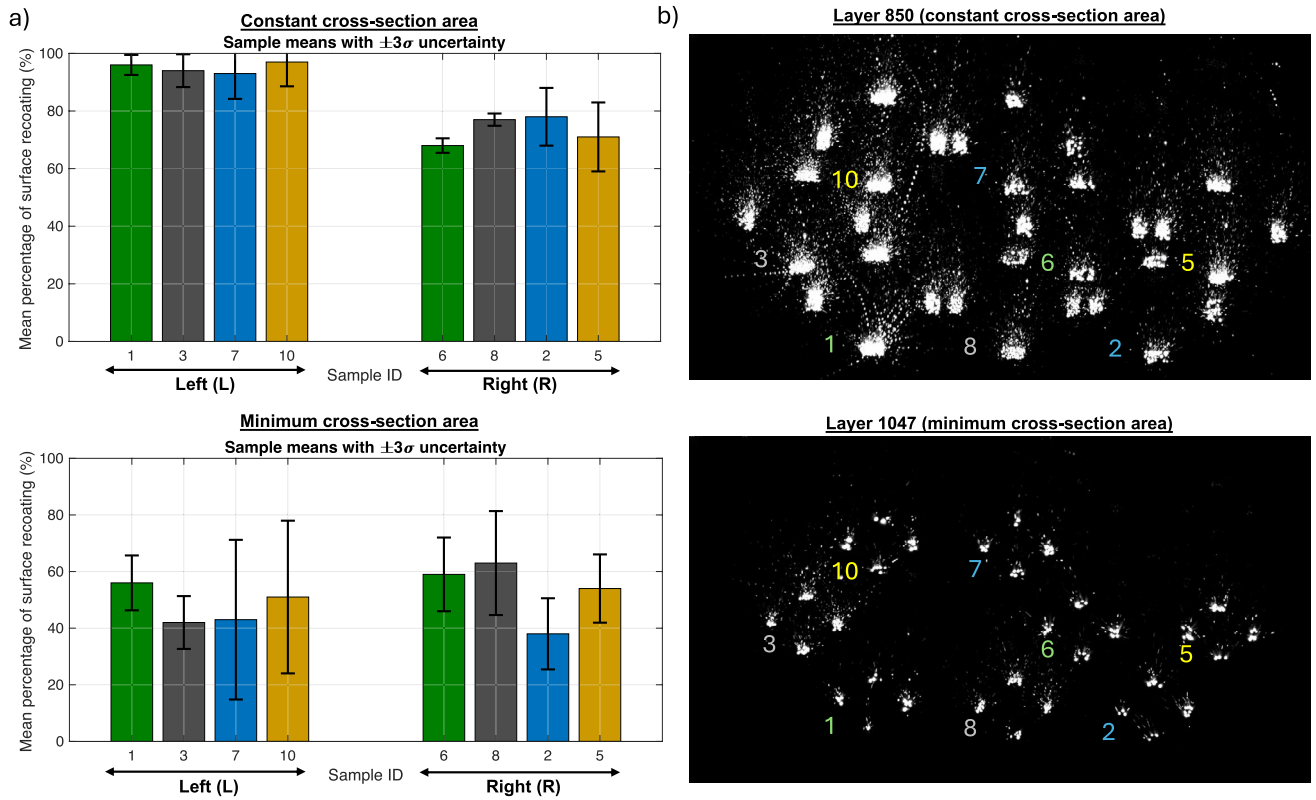

Fig. 5 **a** bar plots with $\pm 3\,\sigma$ intervals of the mean percentage of surface recoating for samples manufactured on the left- and right-hand side of the build area for layers in the range 818 - 964 (top panel) and layers in the range 1036 to 1109 (bottom panel); **b** superimposition of high-speed video frames during the exposure of two different layers: frames were first binarized, then superimposed by assigning a value 1 (white) to pixels labeled as either spatters or LHZ+plume in at least one frame, and 0 (black) to remaining ones; layer 850 is the one with the large cross-section area, layer 1047 is one with minimum cross-section

Table 2 Results of the pairwise statistical comparisons of mean percentages of surface recoating via two-sample Student's *t*-test with familywise significance level of $\alpha = 0.05$ and Bonferroni's correction

Sample (L)	Sample (R)	*p*-value	Significant
Constant cross-section area			
1	6	4.881×10^{-13}	Yes
3	8	5.054×10^{-8}	Yes
10	5	2.447×10^{-7}	Yes
7	2	1.087×10^{-6}	Yes
Minimum cross-section area			
1	6	1.775×10^{-2}	No
3	8	3.614×10^{-5}	Yes
10	5	6.040×10^{-1}	No
7	2	6.523×10^{-1}	No

Sample ID (L) indicates samples on the left-hand side whereas Sample ID (R) indicates samples on the right-hand side

within-layer spatial variability and across-layer variability related to cross-section changes.

Figure 5b shows the superimposition of binarized high-speed video frames acquired during the exposure of all samples in two representative layers: one with nearly constant cross-section area (top panel) and one with minimum cross-section area (bottom panel). A clear decrease in spatter ejections is observed from the former to the latter. In the top panel, the location effect is also visible, with more intense spattering on the left-hand side, whereas it becomes hardly visible at minimum cross-section. This can be interpreted as follows. In the absence of a powder layer, the ejection of loose powder particles entrained by the vapor-driven flow is inherently reduced, and the observed ejecta are therefore predominantly associated with material expelled directly from the melt pool [8, 28]. Conversely, when a sufficiently thick powder layer covers and surrounds the interaction zone, powder entrainment represents a major contribution to the observed spatter population [8]. Accordingly, a reduced powder-layer thickness or local lack of powder recoating on super-elevated areas decreases the amount of loose powder available for entrainment, thereby potentially reducing this contribution to the overall spatter population.

The correlation structure among the in situ estimated features is shown in Fig. 6, where L denotes samples manufactured on the left-hand side of the build area, characterized by more homogeneous powder spreading, and R denotes the right-hand side.

Each point in Fig. 6 corresponds to layer-wise average values of LHZ+plume area, near-origin spatter size, total near-origin spatter number, and near-origin spatter rate. Positive correlations are observed among several descriptors when energy density levels are considered separately. As expected, spatter rate is strongly correlated with spatter number. The figure also indicates differences between parts produced with the same energy density but at different build locations, which are analyzed in detail below.

Before considering location and geometry-induced effects, the influence of controlled process parameters was assessed by aggregating layers and locations. Figures 7, 8, and 9 report 95% confidence intervals for the mean descriptors as functions of LED, laser power, and scan speed, respectively.

Figures 7 and 8 show that the average LHZ+plume area and near-origin spatter size increase with laser power, while no linear dependence on LED is observed. Higher power increases the energy input per unit time, enlarging the melt pool and heat-affected region, whereas scan speed mainly affects heat exposure duration. The 60 W conditions (0.6 J/mm at 100 mm/s and 0.15 J/mm at 400 mm/s) produced the smallest LHZ+plume areas, suggesting limited heat penetration regardless of energy density. Conversely, despite similar energy densities, the 140 W–400 mm/s condition (0.35 J/mm) resulted in larger LHZ+plume regions than the 100 W–250 mm/s condition (0.4 J/mm).

These results indicate that, in PBF-LB/M of NiTi, laser power is the main driver of LHZ size and ejecta dimensions. They also confirm that energy density alone is not a fully reliable descriptor for comparing process states, consistently with previous observations on other PBF-LB/M materials [29–31].

Conversely, Figs. 7, 8, and 9 show that near-origin spatter number and rate decrease as LED increases, mainly due to the effect of scan speed. Previous experimental and numerical studies have shown that spatter ejection dynamics are strongly coupled with vaporization, recoil pressure, vapor-plume-induced entrainment, and melt-pool dynamics [8, 9, 12]. In particular, high-speed imaging studies have reported an increase in average spatter ejection velocity with increasing energy input [10, 28]. Being fixed the laser power, varying the scan speed has been also shown to significantly affect vapor-plume behavior, process stability, and spatter generation [28]. These observations support the interpretation that process conditions promoting more intense vaporization and melt-pool dynamics can increase the velocity of process ejecta. Faster ejecta have a shorter residence time within the near-origin region and are therefore less likely to be captured with the proposed approach. Overall, the near-origin spatter rate appears more effective than the spatter number in capturing these differences, as it shows lower variability and better separates different energy inputs.

In addition to controlled parameters, spatial location and cross-section variation along the build direction induced statistically significant changes in the monitored quantities.

Figure 10 reports 95% confidence intervals for the descriptors of paired NiTi dampers produced with the same

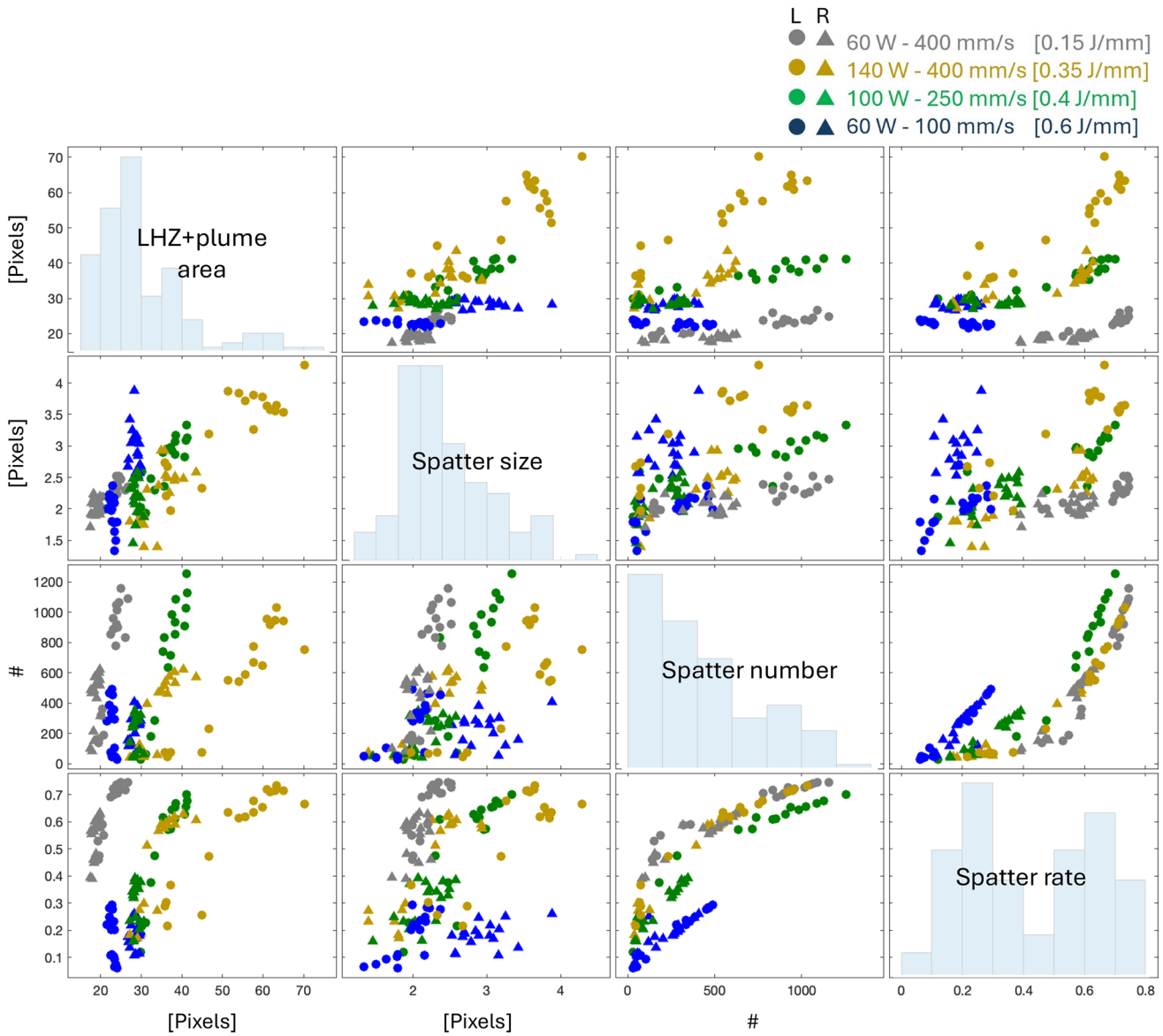

Fig. 6 Scatter plot among pairs of quantities estimated in situ, namely the average LHZ+plume area, the average size of near-origin spatters, the number of near-origin spatters, and the near-origin spatter rate; different colors correspond to different sets of process parameters, whereas different symbols correspond to left and right locations within the build area

LED but located on the left (L) or right (R) side of the build area. Spatial location affected all monitored quantities. In particular, right-hand-side samples showed significantly smaller LHZ+plume areas and near-origin spatter sizes for all tested energy densities. They also showed lower near-origin spatter numbers and rates, although these differences were not statistically significant for all energy levels.

This behavior is consistent with a thinner and discontinuous powder layer on the right-hand side. Faster energy penetration into the underlying solid, which has higher thermal conductivity than loose powder, may lead to smaller and shallower melt pools, explaining the reduced LHZ+plume area. Moreover, less loose powder is available to be entrained by the vapor plume or expelled by recoil pressure, while a shallower melt pool may generate fewer molten ejections [8]. We hypothesize that these mechanisms explain the observed reduction in spatter size, number, and rate.

Gas-flow effects may also contribute to the spatial location effect. However, since all samples were built in a small central region and the analysis focused on near-origin spatters, their influence is expected to be secondary. Nevertheless, convective cooling from the shielding gas can affect LHZ dimensions, such that samples closer to the gas inlet may experience enhanced heat dissipation and reduced thermal accumulation. For NiTi, which is highly sensitive to

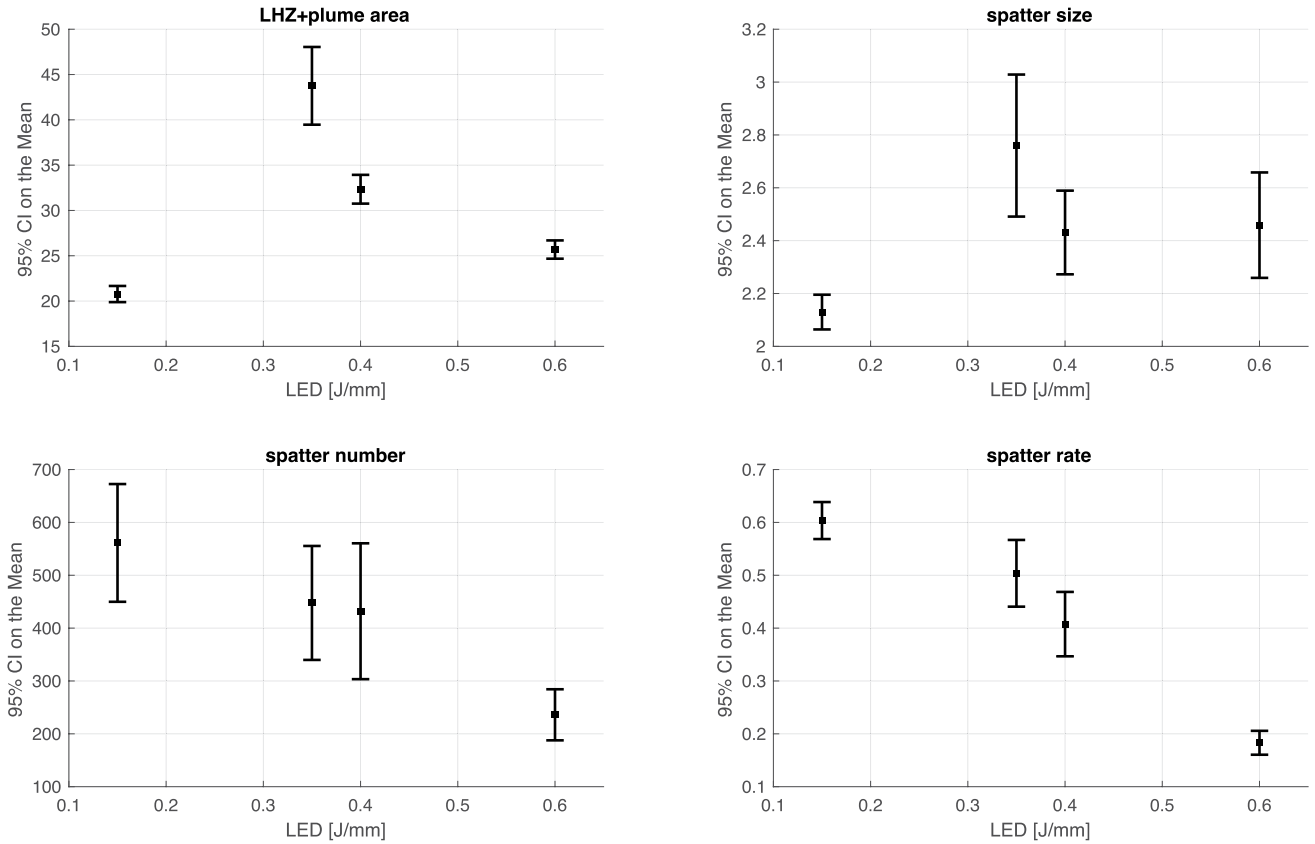

Fig. 7 95% confidence intervals of the mean descriptors (LHZ+plume area, spatter size, spatter number, and spatter rate) as a function of LED

process variations, this effect may add to the mechanisms described above.

Variations along the build direction were also observed. Figure 11 reports the mean LHZ+plume area and near-origin spatter number across layers. The first 11 monitored layers correspond to a nearly constant and maximum cross-section within the octahedral cell, while the following layers correspond to the minimum cross-section region, with only small layer-to-layer variations.

Figure 11 shows that both descriptors change when moving from constant to minimum cross-section.

In the minimum cross-section region, differences between paired samples produced with the same energy density but in different locations decreased for all monitored descriptors. For LHZ+plume area, this effect was most evident at LED = 0.15, 0.35, and 0.4 J/mm, whereas it was less pronounced or absent at LED = 0.6 J/mm. In the former cases, the LHZ+plume area of left-hand-side samples decreased at minimum cross-section, approaching the values of right-hand-side samples. As discussed above, insufficient recoating mainly affected right-hand-side samples in layers 818–964, whereas in layers 1036–1109 it extended to all samples, mitigating location effects. When the cross-section increased again in the last monitored layers, the left–right gap in LHZ+plume area started to widen.

A similar trend was observed for near-origin spatter number. At all energy density levels, spatter number and rate decreased at the smallest cross-section, and the differences between left- and right-hand-side samples were reduced or vanished. This is consistent with lack of recoated powder on all samples, which reduced the ejection of powder particles and droplets from the melt pool.

3.2 Ex situ characterization

Figure 12 summarizes internal porosity and cracks across all samples, with pairs arranged from top to bottom in increasing laser power.

The ex situ characterization shows a strong dependence of defect morphology and severity on both process parameters and spatial location. Samples 3 and 8, produced at the lowest energy density (LED = 0.15 J/mm), exhibit severe cracking at different build heights and limited lack-of-fusion porosity mainly at corners, but the right-hand-side sample shows fewer and less pronounced cracks. Figure 13a compares these two samples in terms of overall number of cracks counted in the respective CT scans. The comparison highlights that sample 3, manufactured on the left-hand side of the build area, exhibited three times more cracks than sample 8, manufactured on the right-hand side. This may

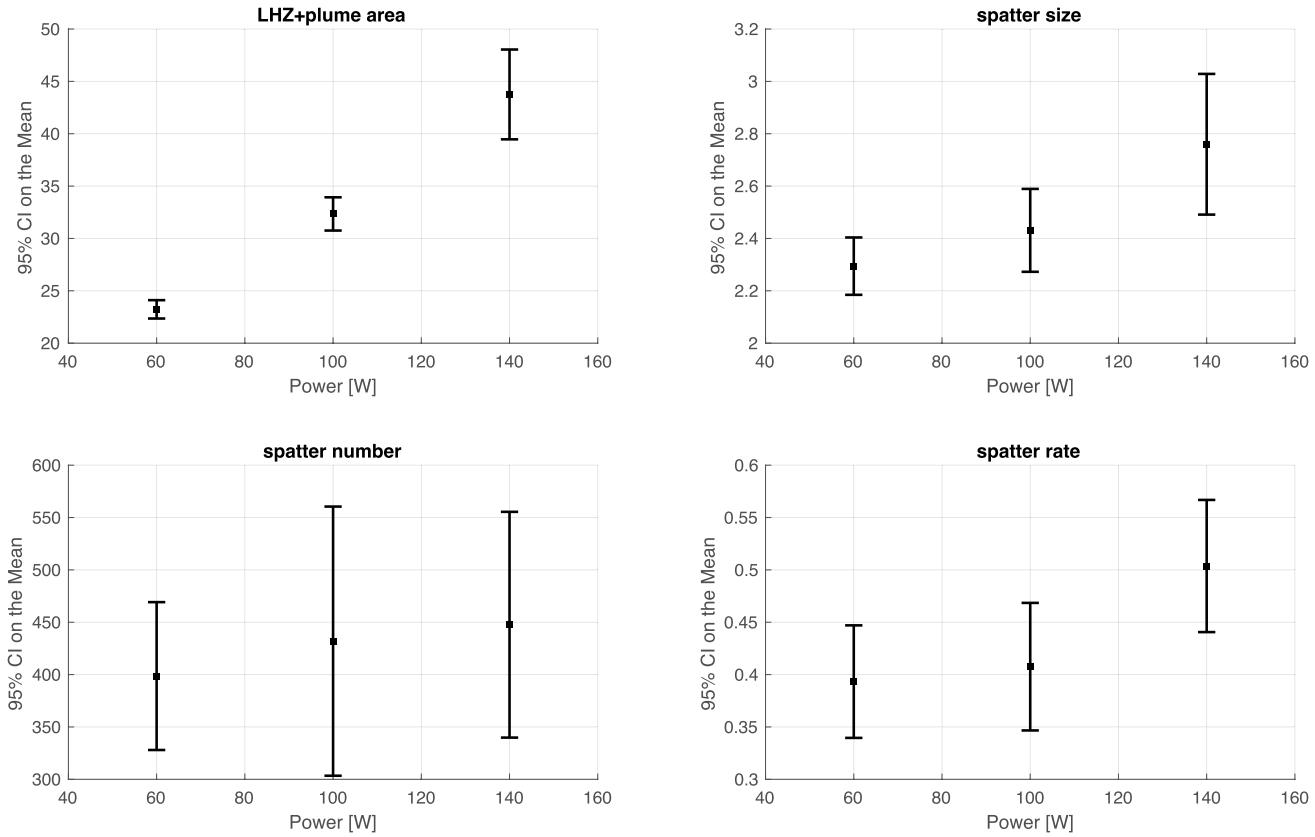

Fig. 8 95% confidence intervals of the mean descriptors (LHZ+plume area, spatter size, spatter number, and spatter rate) as a function of laser power

be interpreted as follow. Local incomplete recoating over super-elevated regions may expose previously consolidated material to the subsequent laser scan, thereby promoting partial remelting of the underlying material instead of melting a complete newly deposited powder layer. Although not directly demonstrated by the present measurements, we hypothesize that such local remelting may have a healing effect on pre-existing cracks or crack-prone regions. This interpretation is consistent with previous studies showing that remelting can reduce cracking in PBF-LB/M materials [32].

Figure 13b, c and d compares the porosity measured in the remaining pairs of samples. It should be noted that the reported porosity values represent an approximate estimate of the true porosity, as defects smaller than approximately 50 µm to 100 µm cannot be reliably detected with the voxel size and acquisition settings adopted in this study. Furthermore, imaging artifacts cannot always be unambiguously distinguished from real pores. Nevertheless, identical CT acquisition parameters and post-processing procedures were applied to all samples, aiming at keeping any measurement bias consistent across the dataset.

It is also worth noticing that, although pore morphology from X-ray CT alone does not allow a unique identification of the underlying formation mechanism, we hypothesize a lack-of-fusion mechanism in the presence of more irregular pores and a keyhole or overheating phenomenon as root cause for more spherical pores. The following discussion relies on these hypotheses, but further validation would be required.

Samples 2 and 7, produced at $P = 60$ W and higher energy density (LED = 0.6 J/mm), do not show cracking but exhibit substantially higher internal porosity. The right-hand-side sample presents a much higher and more diffuse porosity, especially in the octahedral region. Visual inspection also revealed pronounced oxidation in overhanging areas and reduced cross-section regions.

Samples produced at $P = 100$ W and LED = 0.4 J/mm show widespread porosity, with location-dependent size and morphology. The left-hand-side sample (sample 1) contains elongated lack-of-fusion pores aligned with the scan direction, whereas the right-hand-side sample (sample 6) contains more numerous, smaller, and more spherical pores, suggesting keyhole or overheating regimes.

Samples produced at $P = 140$ W and LED = 0.35 J/mm exhibit diffuse irregular porosity, more severe in the right-hand-side sample. The left-hand-side sample (sample 10) shows a higher pore concentration in corner regions and

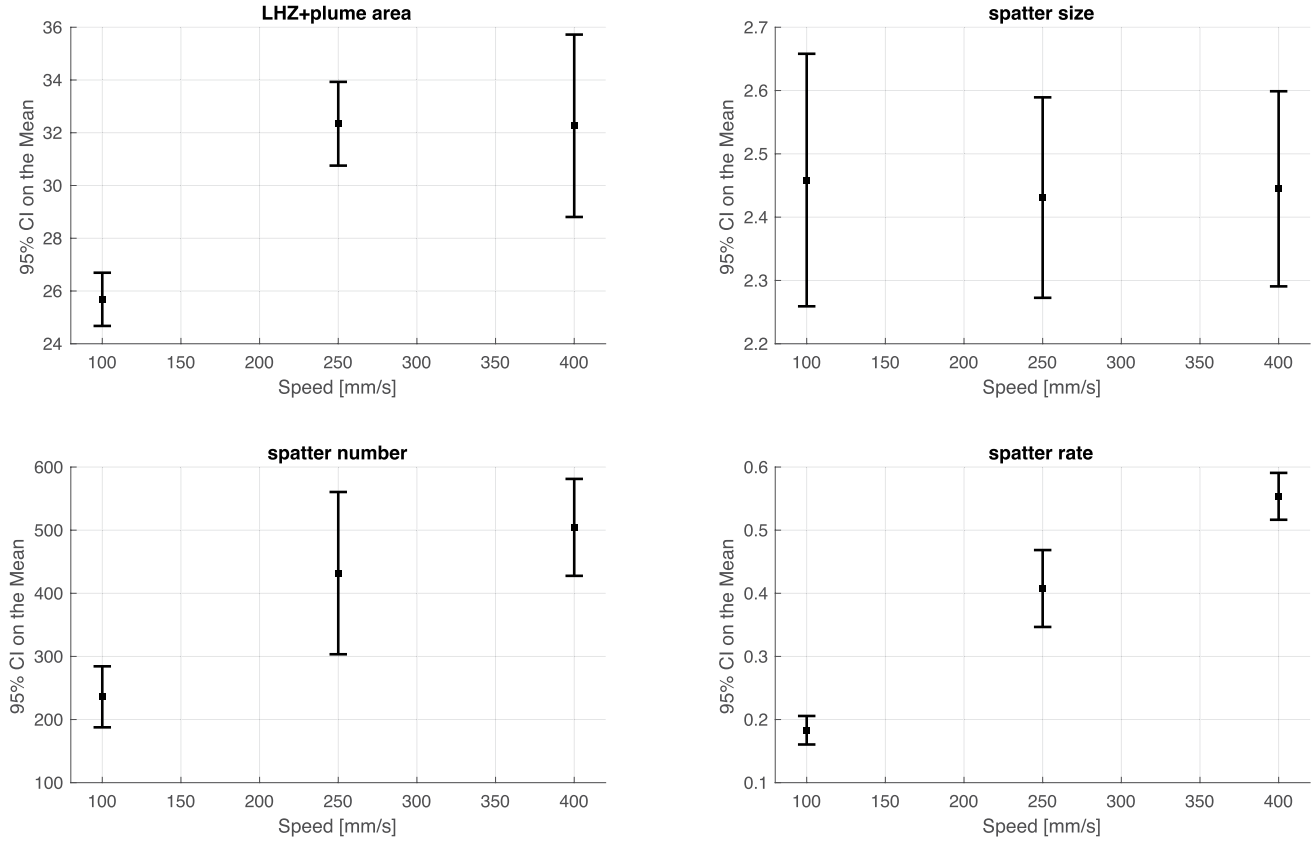

Fig. 9 95% confidence intervals of the mean descriptors (LHZ+plume area, spatter size, spatter number, and spatter rate) as a function of scan speed

reduced cross-section areas, together with some cracks at the base.

Overall, Fig. 13b, c and d quantifies the higher porosity observed in samples manufactured on the right-hand side of the build area.

Geometry-induced variability is also evident, as reduced cross-section regions within the octahedral cell show increased defect concentration, especially in samples 5, 10, and 1. This is consistent with shorter inter-layer cooling time and local heat accumulation, leading to overheating, swelling, and melt-pool instability.

Figure 13 presents an example of the pore volume distribution along the build direction for Sample 10. The figure indicates that porosity is not uniformly distributed throughout the sample height, but is instead concentrated in specific regions. In particular, a pronounced increase in pore volume is observed at the base of the octahedral cell. A further increase is evident within the monitored portion of the build, as the cross-sectional area progressively decreases from the constant cross-section region to the minimum cross-section region. Interestingly, the portion of the sample located above the octahedral cell also exhibits higher porosity than the region below it, despite both sections having the same nominal cross-sectional area. This observation suggests the presence of an additional source of process variability, possibly associated with the progressive accumulation of heat during the build. Although this hypothesis requires further investigation, it highlights the potential influence of build history on the local process conditions and the resulting defect distribution.

The ex situ observations in Figs. 12, 13 and 14 highlight that the location-dependent and geometry-dependent variations detected by in situ spatter-based monitoring translate into changes in defect type, morphology, and spatial distribution, supporting the hypothesis that proposed process signatures may be used as indicators of undesired process variations and their impact on part quality.

Some samples also exhibit a layer-wise discontinuity in internal porosity in the lower half of the octahedral cell, as clearly visible in Fig. 14 slightly above z = 20 mm. This corresponds to the layer where the process was paused to suppress samples 4 and 9, whose excessive energy input caused severe surface superelevation that could interfere with recoating. The discontinuity is more evident in samples 1, 6, 10, and 5, produced with higher power levels. In these samples, localized high porosity in the paused layer was likely caused by the extended inter-layer cooling time, which lowered the melt pool temperature when scanning resumed and

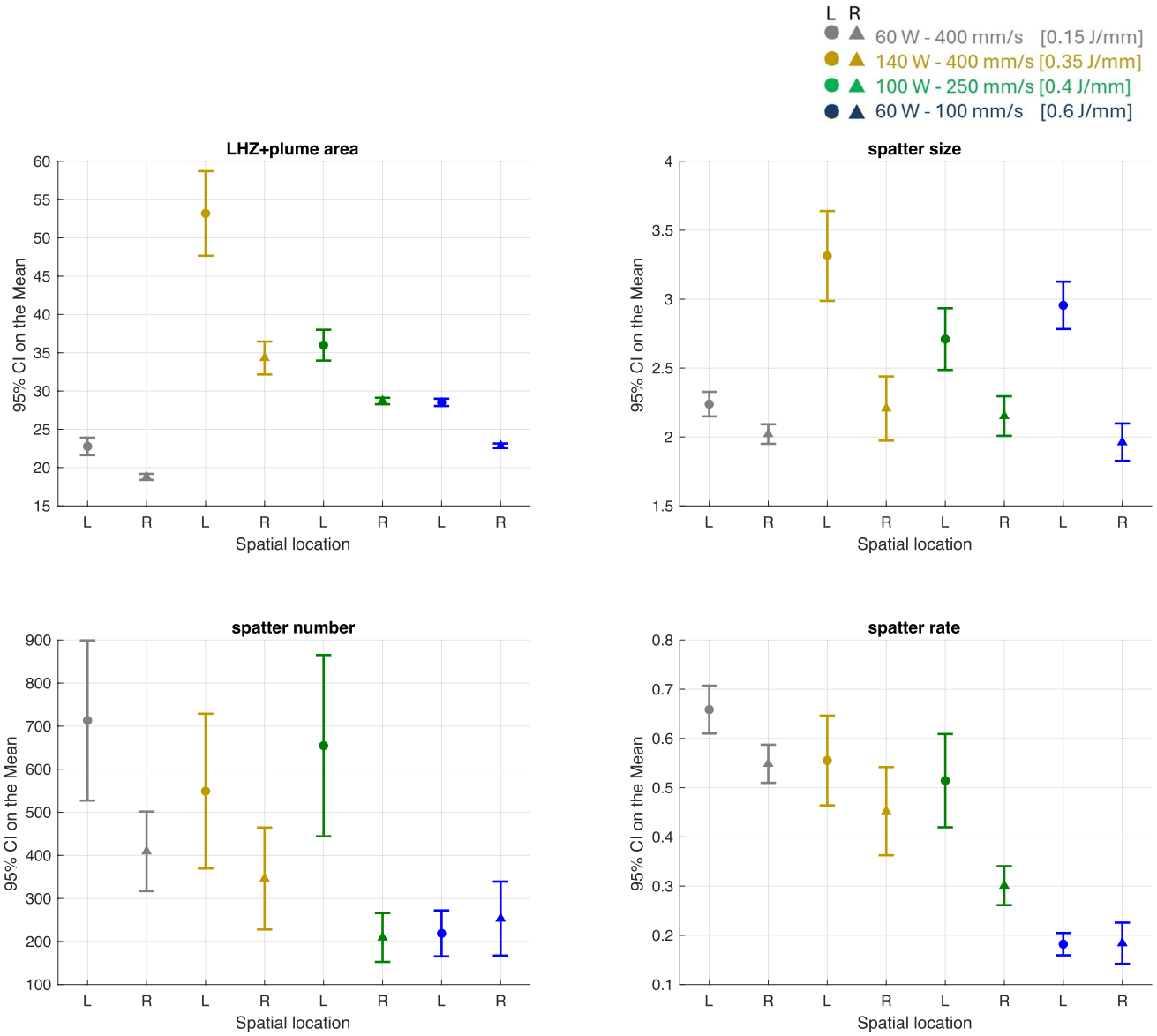

Fig. 10 95% confidence intervals of the mean descriptors (LHZ+plume area, spatter size, spatter number, and spatter rate) as a function of the individual location in the build area, where L stands for left-hand side and R for right-hand side); different colors correspond to different sets of process parameters, whereas different symbols correspond to left and right locations within the build area

promoted lack-of-fusion pores. Increased porosity in subsequent layers may reflect the resulting change in thermal regime.

3.3 Statistical modeling

Building on the qualitative agreement between in situ signatures and defect distributions, logistic regression was used to quantify the relevance of spatter-related features as predictors of undesired process variations. Two sources of variability were considered: location-dependent effects within the build area and geometry-induced variations along the build direction.

Logistic regression estimates the probability of a binary outcome as a function of input variables [33], modeling the log-odds as a linear combination of predictors and enabling interpretable assessment of feature relevance. In this study, the probability of a binary outcome was modeled as

$$\mathbb{P}(Y = 1 \mid \mathrm{x}) = \frac{1}{1 + \exp(-\mathrm{x}^\top \boldsymbol{\beta})}, \tag{1}$$

where $\mathrm{x} \in \mathbb{R}^p$ is the predictor vector and $\boldsymbol{\beta} \in \mathbb{R}^p$ the coefficient vector.

Two binary classification problems were defined. In Model 1, $Y = 1$ denotes samples located on the left-hand

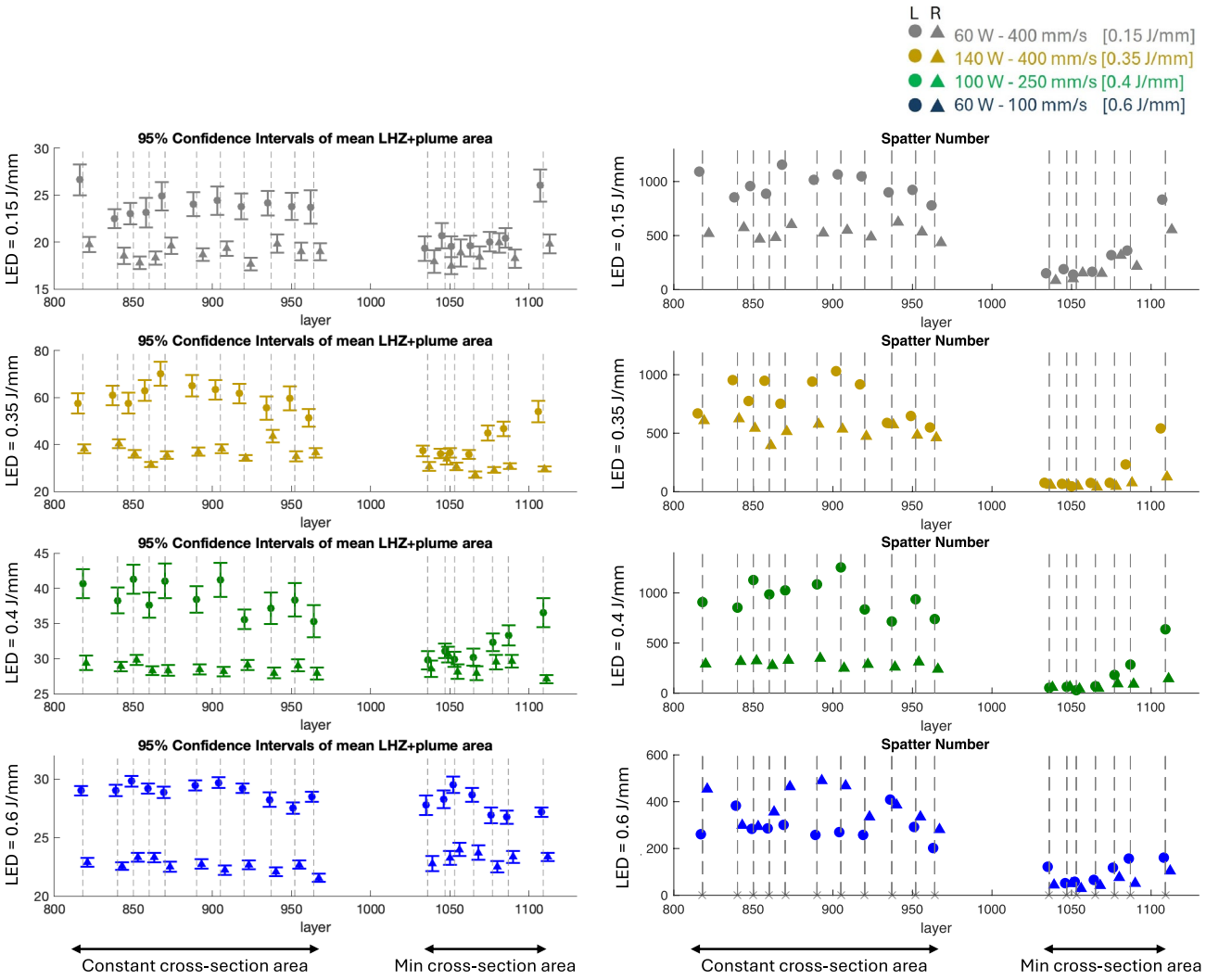

Fig. 11 Left panel: 95% confidence intervals of the mean LHZ+plume area in different layers and with different sets of process parameters; right panel: overall number of near-origin spatters ejected in different layers and with different sets of process parameters; different colors correspond to different sets of process parameters, whereas different symbols correspond to left and right locations within the build area

side and $Y = 0$ those on the right-hand side. In Model 2, $Y = 1$ denotes layers with constant and relatively large cross-section area (first 11 layers), while $Y = 0$ denotes layers with reduced cross-section area (remaining 7 layers). In both cases, x included the spatter-related descriptors extracted from in situ monitoring data. Each observation corresponds to the four in situ descriptors computed for one individual part within one monitored layer. The sample size used in the analysis consists of 18 monitored layers for each of 8 samples, for a total of 144 part-layer observations.

Table 3 summarizes the binary response and accuracy of each model. A leave-one-out cross-validation procedure was applied, in which each observation was excluded in turn. Both logistic regression models were fitted using all remaining observations and used to predict the class of the excluded observation. Predictor standardization was also performed independently within each training fold, so that the excluded observation does not contribute to either model fitting or predictor scaling.

The descriptors were more effective in discriminating cross-section-related process conditions (93.75% accuracy) than location-dependent effects (77.78% accuracy).

Figure 15 shows a Pareto analysis of the relative magnitude of standardized logistic regression coefficients. $\pm 3\,\sigma$ error bars are shown, where σ is the sample standard deviation of the standardized coefficient in different cross-validation runs. These error bars are thus intended as a descriptive measure of the sensitivity of the estimated coefficient magnitudes to changes in the observations used for model fitting.

Figure 15 shows that there are dominant coefficients in each model, whereas the relatively small variability of the coefficients across cross-validation folds indicates that

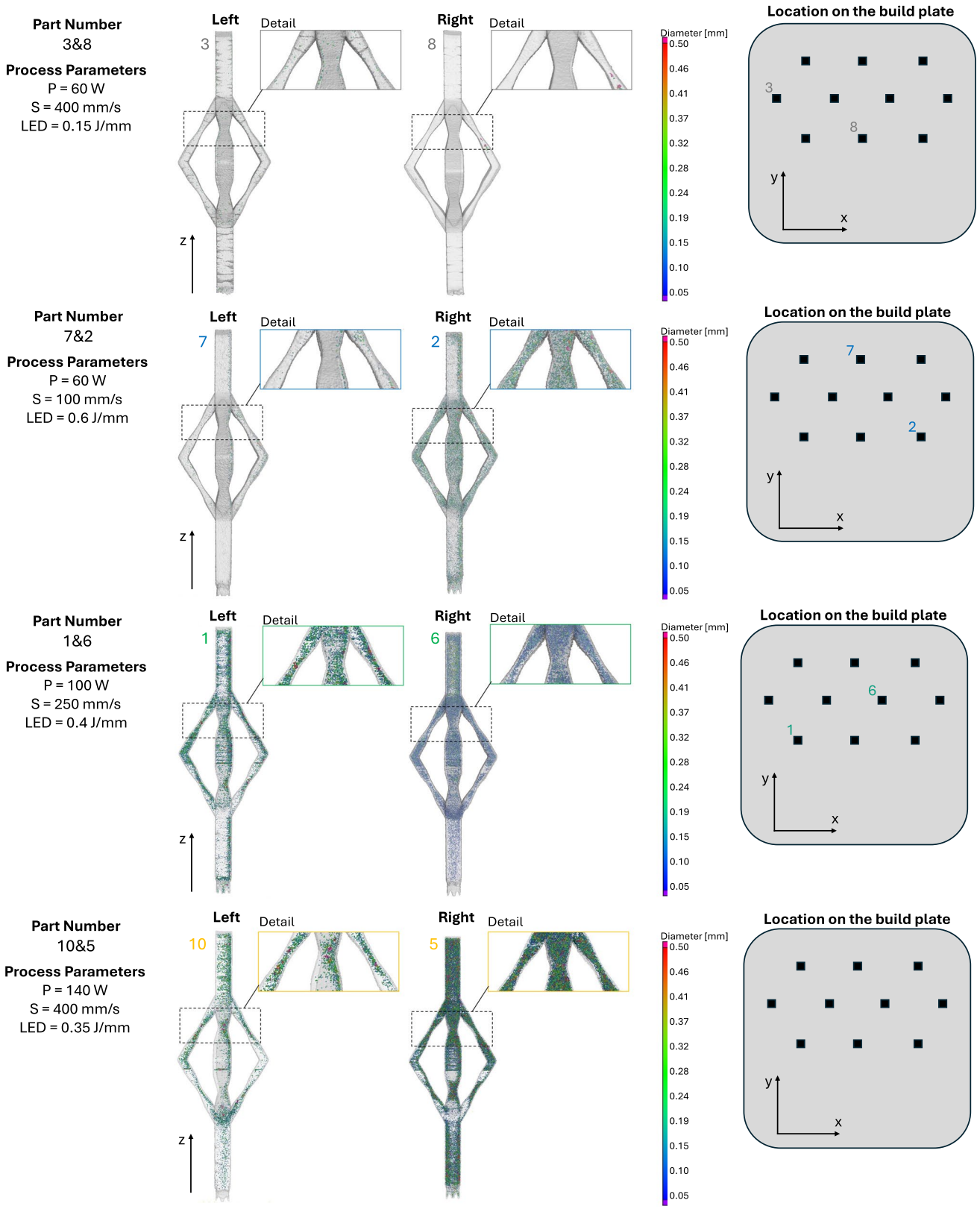

Fig. 12 Synthetic representation of the X-ray CT characterization of as-built samples; The figure shows: (1) a front view of the pore and crack locations in each sample, where the color bar indicates the equivalent diameter of detected pores; a detail, for each sample, corresponding to the monitored portion of the build; a scheme of sample location within the build area. Samples are paired based on their associated process parameters

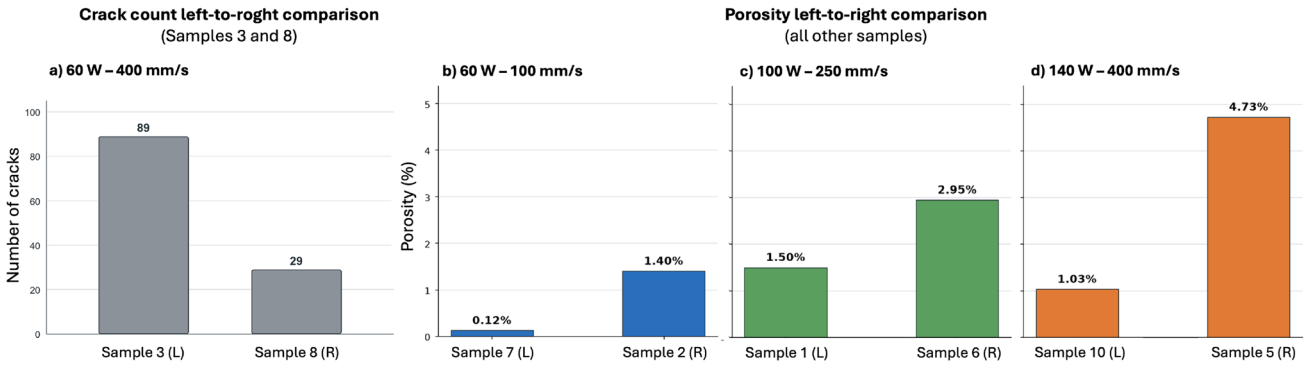

Fig. 13 **a** Left-to-right comparison between samples 3 and 8 in terms of number of cracks counted in the respective CT scans; **b**–**d** Left-to-right comparison in terms of porosity (%) estimated in different pairs of samples manufactured with the same sets of process parameters

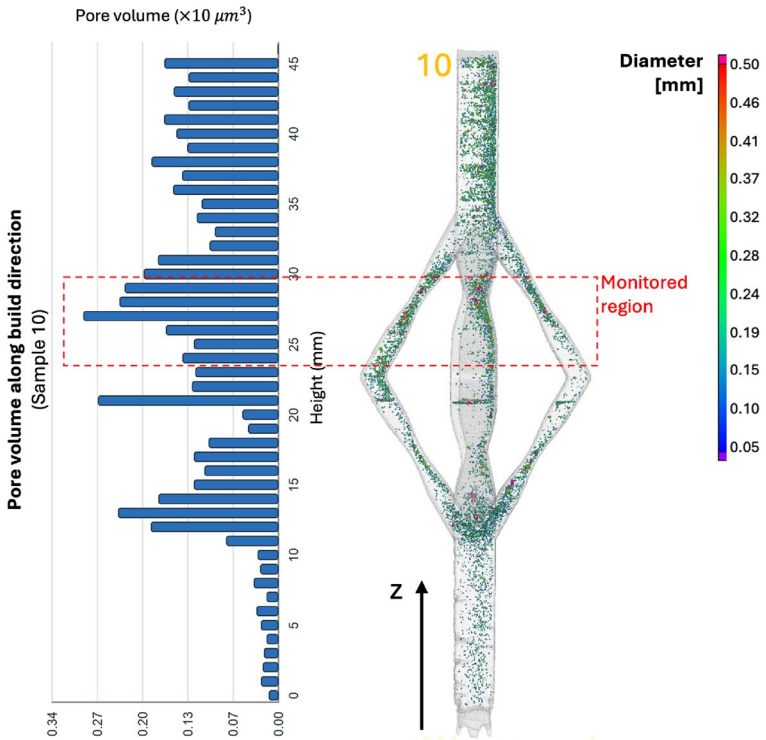

Fig. 14 Example of the pore volume variation along the build direction for sample 10. The red rectangle indicates the portion of the build where in situ monitoring was performed (it should be noted that the vertical scale in the right panel refers to the CT scan acquired after the sample had been removed from the build plate. Consequently, the reported height does not exactly correspond to the original build height during the build). The pore diameter scale is shown on the right

Table 3 Leave-one-out cross-validation accuracy of logistic regression models using four in situ computed descriptors as predictors

Logistic regression model	Binary response	Accuracy (%)
Model 1	Location within the layer (LEFT vs RIGHT)	77.78
Model 2	Cross-section along z (LARGE vs SMALL)	93.75

these patterns are stable with respect to the exclusion of individual observations. For Model 1, spatter size exhibits a markedly larger coefficient magnitude than the remaining descriptors, indicating the strongest conditional association with the response. For Model 2, spatter number and rate exhibit the largest coefficient magnitude, instead. However, the correlation between spatter number and spatter rate indicates that these descriptors contain partially overlapping information. Consequently, taken together, the results indicate that descriptors related to the amount of spatter ejection, expressed in terms of either spatter number or spatter rate, show the strongest conditional association with the response within Model 2.

These results confirm that spatter-related quantities capture undesired process changes with potential impact on final part quality. Therefore, monitoring both the size and quantity, or rate, of near-origin spatters potentially enables the detection of distinct process dynamics and anomalies arising from different mechanisms.

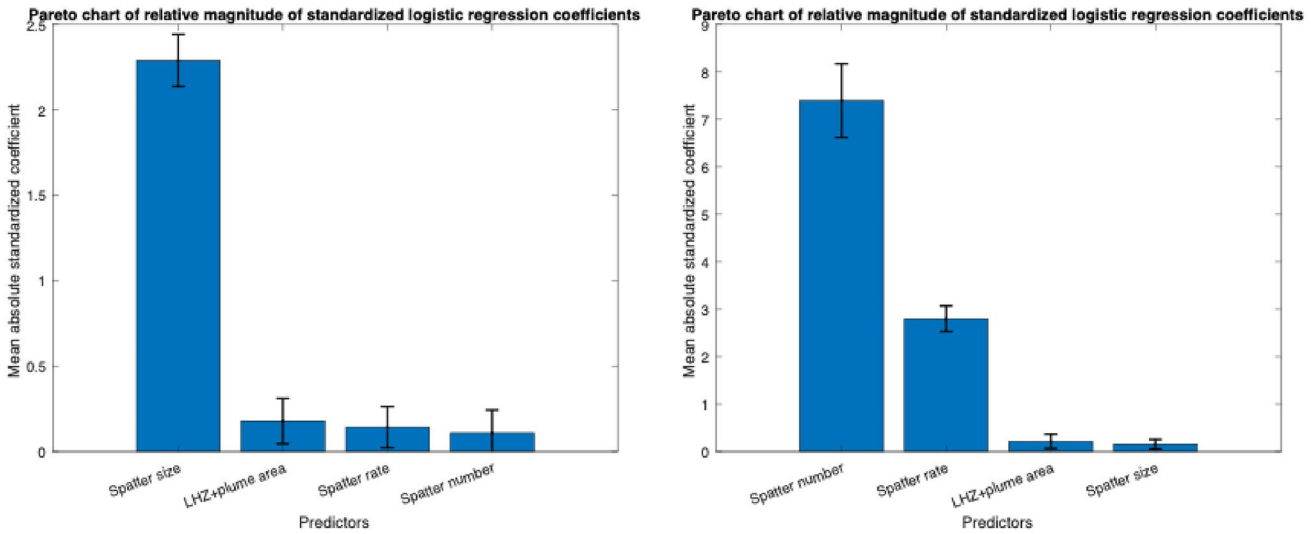

Fig. 15 Pareto plot to evaluate the relative magnitude of standardized logistic regression coefficients for individual predictors in the logistic regression Model 1 (left) and Model 2 (right) with $\pm 3\,\sigma$ error bars

3.4 Discussion

The results show that spatter-related descriptors provide information that is not fully captured by the LHZ+plume area alone, in agreement with previous studies on more conventional materials [10]. While the LHZ+plume area mainly reflects the extent of the thermally affected region and is strongly driven by laser power, spatter properties are more sensitive to additional sources of variability, including location-dependent powder spreading and geometry-induced effects along the build direction. In particular, different descriptors capture distinct aspects of the process: size-related features reflect local thermal conditions, whereas occurrence-based metrics, especially spatter rate, are more sensitive to geometry-driven variations.

The proposed near-origin spatter approach enables robust extraction of process signatures under industrially representative conditions. By focusing on spatters detected close to their point of origin, the method improves the association between spatter events and local process conditions, while reducing mislabeling and repeated counting in complex builds with multiple parts and overlapping thermal emissions. Compared to full spatter tracking, which often requires controlled acquisition conditions, this approach is transferable to practical PBF-LB/M environments, including multi-laser systems.

Some limitations should be acknowledged. Restricting the analysis to near-origin spatters neglects information related to faster ejecta and their trajectories, which may be relevant for characterizing recoil pressure and melt pool instability. In addition, the observation radius requires calibration and may depend on the optical setup, while perspective distortions and out-of-focus effects may affect measurement accuracy. The use of visible-range imaging also prevents full separation of melt pool, plume, and surrounding heated regions.

Overall, the results highlight that part quality in PBF-LB/M is governed by the interaction of multiple variability sources. Spatter monitoring may be suitable to capture a variety of phenomena, but it should be considered a complementary tool rather than a standalone solution. Its integration with other sensing modalities, such as powder bed imaging, melt pool monitoring, and thermography, can provide a more complete understanding of defect formation mechanisms.

These aspects are particularly relevant for materials such as NiTi, characterized by a narrow process window and high sensitivity to local thermal conditions. In this context, spatter-based descriptors provide indirect yet sensitive indicators of variations in energy input and melt pool dynamics, supporting process understanding and optimization.

4 Conclusions

This study investigated the role of spatter-based descriptors in providing effective in situ indicators of process variability in PBF-LB/M of NiTi, capturing effects that are not fully described by conventional metrics such as LHZ+plume area or energy density.

The main findings can be summarized as follows:

- Spatter monitoring enables the detection of process variations beyond nominal process parameters, including location-dependent powder spreading and geometry-induced effects along the build direction;

- Near-origin spatter analysis allows robust and physically meaningful process signatures to be extracted under complex and industrially representative conditions;
- Different spatter descriptors provide complementary information, with size-related features capturing local thermal conditions and occurrence-based metrics capturing geometry-driven variations;
- Energy density alone is not sufficient to explain the mechanisms governing in situ signatures and resulting defect formation;
- The observed in situ variations are consistent with ex situ CT measurements, confirming their relevance for process monitoring and defect assessment.

Future research may extend the present experimental campaign. Direct measurements of the gas-flow field across the build plate would provide valuable additional information to better assess its possible contribution to location-dependent effects. Such spatially resolved characterization may be explored to further disentangle the effects of recoating conditions and gas-flow dynamics on the observed process signatures. Further investigation may be devoted to the influence of the powder's PSD on the size, number, and ejection behavior of process ejecta across different builds and powder batches. Future work will also extend the analysis to multi-sensor monitoring approaches, combining high-speed imaging with thermography, powder bed imaging, and melt pool monitoring.

Although demonstrated on NiTi, the proposed approach is expected to be transferable to other material systems, particularly those with narrow processing windows or strong sensitivity to local thermal variations.

Acknowledgements This research was supported by ACCORDO Quadro ASI-POLIMI - Attività di Ricerca e Innovazione n. 2018-5-HH.0, collaboration agreement between the Italian Space Agency and Politecnico di Milano.

Author contributions H.Z., M.G.: data curation, methodology, investigation, formal analysis, validation, writing, reviewing and editing; T.B., A.N., A.M.G., P.B.: investigation, conceptualization, methodology, validation, writing, reviewing and editing; G.S., B.M.C.: supervision, conceptualization, methodology, validation, reviewing and editing.

Funding Open access funding provided by Politecnico di Milano within the CRUI-CARE Agreement.

Data availability Data can be made available by the authors upon request.

Declarations

Conflict of interest The authors declare no conflict of interest.

Open Access This article is licensed under a Creative Commons Attribution 4.0 International License, which permits use, sharing, adaptation, distribution and reproduction in any medium or format, as long as you give appropriate credit to the original author(s) and the source, provide a link to the Creative Commons licence, and indicate if changes were made. The images or other third party material in this article are included in the article's Creative Commons licence, unless indicated otherwise in a credit line to the material. If material is not included in the article's Creative Commons licence and your intended use is not permitted by statutory regulation or exceeds the permitted use, you will need to obtain permission directly from the copyright holder. To view a copy of this licence, visit http://creativecommons.org/licenses/by/4.0/.

References

1. Donmez A, Fox J, Kim F, Lane B, Praniewicz M, Tondane V, Weaver J, Witherell P (2024) In-process monitoring and non-destructive evaluation for metal additive manufacturing. NIST Internal Report 8538, National Institute of Standards and Technology (NIST). https://doi.org/10.6028/NIST.IR.8538
2. ASTM International (2023) Strategic guide: Additive manufacturing in-situ monitoring technology readiness - findings and path forward for application in qualification and certification. Technical report, ASTM International, Additive Manufacturing Center of Excellence
3. Grasso M, Remani A, Dickins A, Colosimo BM, Leach RK (2021) In-situ measurement and monitoring methods for metal powder bed fusion: an updated review. Meas Sci Technol 32(11):112001. https://doi.org/10.1088/1361-6501/ac0b6b
4. Sing SL, Yeong WY (2020) Laser powder bed fusion for metal additive manufacturing: perspectives on recent developments. Virtual Phys Prototyp 15(3):359–370. https://doi.org/10.1080/17452759.2020.1779999
5. Fang Q, Xiong G, Zhou M, Tamir TS, Yan CB, Wu H, Wang FY (2022) Process monitoring, diagnosis and control of additive manufacturing. IEEE Trans Autom Sci Eng 21(1):1041–1067. https://doi.org/10.1109/TASE.2022.3158452
6. McCann R, Obeidi MA, Hughes C, McCarthy É, Egan DS, Vijayaraghavan RK, Brabazon D (2021) In-situ sensing, process monitoring and machine control in laser powder bed fusion: a review. Addit Manuf 45:102058. https://doi.org/10.1016/j.addma.2021.102058
7. Zhang Y, Yan W (2023) Applications of machine learning in metal powder-bed fusion in-process monitoring and control: status and challenges. J Intell Manuf 34(6):2557–2580. https://doi.org/10.1007/s10845-022-01940-5
8. Ly S, Rubenchik AM, Khairallah SA, Guss G, Matthews MJ (2017) Metal vapor micro-jet controls material redistribution in laser powder bed fusion additive manufacturing. Sci Rep 7(1):4085. https://doi.org/10.1038/s41598-017-04237-z
9. Bidare P, Bitharas I, Ward RM, Attallah MM, Moore AJ (2018) Fluid and particle dynamics in laser powder bed fusion. Acta Mater 142:107–120. https://doi.org/10.1016/j.actamat.2017.09.051
10. Repossini G, Laguzza V, Grasso M, Colosimo BM (2017) On the use of spatter signature for in-situ monitoring of Laser Powder Bed Fusion. Addit Manuf 16:35–48. https://doi.org/10.1016/j.addma.2017.05.004
11. Barrett C, Carradero C, Harris E, Rogers K, MacDonald E, Conner B (2019) Statistical analysis of spatter velocity with high-speed stereovision in laser powder bed fusion. Progress Additive Manuf 4(4):423–430. https://doi.org/10.1007/s40964-019-00094-6
12. Guo D, Lambert-Garcia R, Hocine S, Fan X, Greenhalgh H, Shahani R, Majkut M, Rack A, Lee PD, Alex Leung CL (2024)

Correlative spatter and vapour depression dynamics during laser powder bed fusion of an Al-Fe-Zr alloy. Int J Extreme Manuf. https://doi.org/10.1088/2631-7990/ad4e1d
13. Gobert C, Diewald E, Beuth JL (2024) Spatter detection and tracking in high-speed video observations of laser powder bed fusion. Rapid Prototyp J. https://doi.org/10.1108/RPJ-03-2023-0108
14. Stokes MA, Khairallah SA, Volkov AN, Rubenchik AM (2022) Fundamental physics effects of background gas species and pressure on vapor plume structure and spatter entrainment in laser melting. Addit Manuf 55(April):102819. https://doi.org/10.1016/j.addma.2022.102819
15. Bidare P, Bitharas I, Ward RM, Attallah MM, Moore AJ (2018) Laser powder bed fusion in high-pressure atmospheres. Int J Adv Manuf Technol 99(1–4):543–555. https://doi.org/10.1007/s00170-018-2495-7
16. Bidare P, Bitharas I, Ward RM, Attallah MM, Moore AJ (2018) Laser powder bed fusion at sub-atmospheric pressures. Int J Mach Tools Manuf 130–131(March):65–72. https://doi.org/10.1016/j.ijmachtools.2018.03.007
17. Li F, Bitharas I, Moore AJ, Tan W (2025) Effects of gas composition and pressure level on powder spattering and denudation in laser powder bed fusion. Acta Mater 299:121443. https://doi.org/10.1016/j.actamat.2025.121443
18. Yang Y, Chen Z, Liu Z, Wang H, Zhang Y, Wang D (2023) Influence of shielding gas flow consistency on parts quality consistency during large-scale laser powder bed fusion. Optics Laser Technol 158:108899. https://doi.org/10.1016/j.optlastec.2022.108899
19. Liu Z, Yang Y, Wang D, Ge W, Yan W (2025) Spattering trajectory, residing pattern and trap ratio under various gas flow conditions in large-scale laser powder bed fusion: Experiment and simulation. J Mater Process Technol 343:118995. https://doi.org/10.1016/j.jmatprotec.2025.118995
20. Riva G, Airoldi G, Besseghini S (1995) The step-wise martensite to austenite reversible transformation. Meccanica 30(5):495–503. https://doi.org/10.1007/BF01557081
21. Heller L, Šittner P (2024) On the habit planes between elastically distorted austenite and martensite in NiTi. Acta Mater 269(December 2023):119828. https://doi.org/10.1016/j.actamat.2024.119828
22. Li B, Shen Y, An Q (2020) Structural origin of reversible martensitic transformation and reversible twinning in NiTi shape memory alloy. Acta Mater 199:240–252. https://doi.org/10.1016/j.actamat.2020.08.039
23. Radhamani R, Balakrishnan M (2023) NiTi shape memory alloy: unraveling the role of internal friction in passive damping – a review. Mater Today Commun 37(September):107276. https://doi.org/10.1016/j.mtcomm.2023.107276
24. Lin HC, Wu SK, Yeh MT (1993) Damping characteristics of TiNi shape memory alloys. Metall Trans A 24(10):2189–2194. https://doi.org/10.1007/BF02648593
25. Biasutti T, Bettini P, Grande AM, Sala G, Colosimo BM, Nespoli A (2025) Design and optimization of a new NiTi-based shape memory alloy structures for damping applications via additive manufacturing. Progress Additive Manuf. https://doi.org/10.1007/s40964-025-00962-4
26. Zhu JN, Borisov E, Liang X, Farber E, Hermans MJM, Popovich VA (2021) Predictive analytical modelling and experimental validation of processing maps in additive manufacturing of nitinol alloys. Addit Manuf 38(September 2020):101802. https://doi.org/10.1016/j.addma.2020.101802
27. Xue L, Atli KC, Picak S, Zhang C, Zhang B, Elwany A, Arroyave R, Karaman I (2021) Controlling martensitic transformation characteristics in defect-free NiTi shape memory alloys fabricated using laser powder bed fusion and a process optimization framework. Acta Mater 215:117017. https://doi.org/10.1016/j.actamat.2021.117017
28. Zheng H, Li H, Lang L, Gong S, Ge Y (2018) Effects of scan speed on vapor plume behavior and spatter generation in laser powder bed fusion additive manufacturing. J Manuf Process 36:60–67. https://doi.org/10.1016/j.jmapro.2018.09.011
29. Scipioni Bertoli U, Wolfer AJ, Matthews MJ, Delplanque J-PPR, Schoenung JM, Scipioni U, Wolfer AJ, Matthews MJ, Delplanque J-PPR, Schoenung JM (2017) On the limitations of Volumetric Energy Density as a design parameter for Selective Laser Melting. Mater Des 113:331–340. https://doi.org/10.1016/j.matdes.2016.10.037
30. Deng Q, Wang X, Lan Q, Chang Z, Liu Z, Su N, Wu Y, Liu D, Peng L, Ding W (2022) Limitations of linear energy density for laser powder bed fusion of Mg-15Gd-1Zn-0.4Zr alloy. Mater Charact 190:112071. https://doi.org/10.1016/j.matchar.2022.112071
31. Buhairi MA, Foudzi FM, Jamhari FI, Sulong AB, Radzuan NAM, Muhamad N, Mohamed IF, Azman AH, Harun WSW, Al-Furjan MSH (2023) Review on volumetric energy density: influence on morphology and mechanical properties of Ti6Al4V manufactured via laser powder bed fusion. Progress Additive Manuf 8(2):265–283. https://doi.org/10.1007/s40964-022-00328-0
32. Hu P, Liu Z, Zhang H, Li Y, Zhou Q, Xie J (2024) Effect of remelting on cracking of Inconel 939 fabricated via laser powder bed fusion. Mater Charact 214:114087. https://doi.org/10.1016/j.matchar.2024.114087
33. Hosmer DW Jr, Lemeshow S, Sturdivant RX (2013) Applied logistic regression, 3rd edn. Wiley, Hoboken

Publisher's Note Springer Nature remains neutral with regard to jurisdictional claims in published maps and institutional affiliations.